

# Improved implicit diffusion model with knowledge distillation to estimate the spatial distribution density of carbon stock in remote sensing imagery

Zhenyu Yu<sup>1,\*</sup>

<sup>1</sup>Faculty of Computer Science and Information Technology, Universiti Malaya, Kuala Lumpur, 524005, Malaysia

\*E-mail: yuzhenyuyl@foxmail.com

## ABSTRACT

The forest serves as the most significant terrestrial carbon stock mechanism, effectively reducing atmospheric CO<sub>2</sub> concentrations and mitigating climate change. Remote sensing provides high data accuracy and enables large-scale observations. Optical images facilitate long-term monitoring, which is crucial for future carbon stock estimation studies. This study focuses on Huize County, Qujing City, Yunnan Province, China, utilizing GF-1 WFV satellite imagery. The KD-VGG and KD-UNet modules were introduced for initial feature extraction, and the improved implicit diffusion model (IIDM) was proposed. The results showed: (1) The VGG module improved initial feature extraction, improving accuracy, and reducing inference time with optimized model parameters. (2) The Cross-attention + MLPs module enabled effective feature fusion, establishing critical relationships between global and local features, achieving high-accuracy estimation. (3) The IIDM model, a novel contribution, demonstrated the highest estimation accuracy with an RMSE of 12.17%, significantly improving by 41.69% to 42.33% compared to the regression model. In carbon stock estimation, the generative model excelled in extracting deeper features, significantly outperforming other models, demonstrating the feasibility of AI-generated content in quantitative remote sensing. The 16-meter resolution estimates provide a robust basis for tailoring forest carbon sink regulations, enhancing regional carbon stock management.

## Introduction

Given the increasing threat of global climate change, human activities pose unprecedented challenges to Earth's ecosystems<sup>1</sup>. As a result, forest resource management and use have become primary concerns for researchers and policymakers worldwide<sup>2</sup>. Forest ecosystems provide a variety of ecological services and play a crucial role as regulators of the global carbon cycle, contributing significantly to climate change mitigation<sup>3</sup>. It is imperative to monitor and quantify the temporal and spatial variations in regional carbon stocks to understand the dynamics of forest carbon sources and sinks and to develop effective regulatory strategies<sup>4,5</sup>.

Forest carbon stock monitoring is increasingly integrating ground-based sample data with satellite remote sensing observations<sup>6-9</sup>. While ground monitoring provides precise data, it is hindered by time-consuming and labor-intensive processes, making it impractical for large-scale observations<sup>10,11</sup>. In contrast, remote sensing inversion methods offer a viable solution by overcoming the limitations of sample-based monitoring, enabling more efficient and accurate monitoring with continuous improvements<sup>12,13</sup>. Spectral information-based methods can infer vegetation growth status and identify vegetation types within ecosystems, aiding in estimating carbon stocks. However, despite their high accuracy, these methods often struggle to explore intricate nonlinear relationships due to image quality issues, resulting in limited improvements in estimation accuracy<sup>14</sup>.

Methods based on structural information can directly measure biomass and carbon stock, but their effectiveness is constrained by the resolution and coverage of remote sensing images<sup>10</sup>. Physical model-based approaches estimate the carbon stock by developing carbon-cycle models that simulate the carbon sink and cycle processes within ecosystems. Although this method can account for the variations and complexities of different ecosystems, it requires precise ecological parameters and robust data support<sup>15</sup>. Conversely, machine learning-based methods uncover deeper relationships between image data and carbon stock, enabling rapid and efficient estimates<sup>16,17</sup>. Integrating sample monitoring data with remote sensing data to establish a universal and high-precision remote sensing monitoring model for regional forest carbon stock has become an urgent priority.

In summary, we have successfully reframed the carbon stock estimation problem as an image translation task and utilized the implicit diffusion model as our foundational network structure. Using GF-1 WFV satellite imagery as the primary data source and adapting our methodology to the specific characteristics of Huize County, we achieved precise estimations of the regional carbon stock distribution density. This work provides a critical theoretical foundation for informing forest carbon sink regulation strategies and decision-making. Our main contributions include:

- The VGG module, enhanced through knowledge distillation, was incorporated into the implicit diffusion model for initial feature extraction and to construct the encoder-decoder structure. Similarly, the UNet model was distilled, resulting in a reduction in the number of parameters.
- Attention mechanisms combined with MLP were added for feature fusion, enabling the capture of relationships between local and global features and achieving high-accuracy estimates of carbon stock density distribution.
- The improved implicit diffusion model (IIDM) reduced inference time and enhanced accuracy, with experimental results demonstrating the feasibility of artificial intelligence-generated content (AIGC) in quantitative remote sensing.

## Related work

### Key issues in carbon stock estimation

**Data selection.** Ground monitoring, while providing precise data, is impractical for large-scale observations due to its labor-intensive and time-consuming nature<sup>10,11</sup>. Remote sensing inversion methods mitigate these issues, improving both efficiency and accuracy<sup>12,13</sup>. Among the most promising remote sensing resources for additional data sets are medium-resolution (10~30 m) optical data. The long operational lifetimes of these satellites make them ideal for continuous monitoring of forest dynamics<sup>18</sup>. When utilizing multispectral images as data sources, carbon stock calculations have mainly focused on estimating biomass and stock, with relatively few studies directly estimating carbon stock from image data.

**Method selection.** Zhang et al.<sup>19</sup> combined ground observations, MODIS, GLAS, climate, and terrain data with the random forest algorithm to generate a 1 km resolution aboveground biomass map for China, achieving an interpretability of 75% and an RMSE of 45.5 Mg/ha. Puliti et al.<sup>18</sup> estimated the total change in forest aboveground biomass over approximately 1.4 million hectares in northern Norway using National Forest Inventory (NFI), Sentinel-2, and Landsat data. Chopping et al.<sup>20</sup> estimated aboveground biomass in the southwestern U.S. from 2000 to 2015 using the Multi-angle Imaging Spectro Radiometer (MISR), achieving an RMSE of 37.0 Mg/ha. Despite the detailed spatial features and rich surface texture information provided by medium-resolution remote sensing images, these images typically have limited spectral bands, and existing carbon stock data products usually exhibit low resolution. Therefore, the key to accurately estimating carbon sinks lies in developing effective algorithms capable of extracting deep-seated features.

### Challenges for quantitative remote sensing

One of the most significant challenges in quantitative remote sensing is effectively managing complex non-linear relationships to improve data accuracy<sup>21,22</sup>. Although remote sensing inversion methods can efficiently monitor and estimate forest carbon stocks, they still face obstacles such as poor image quality and complex identification of vegetation growth and types. Consequently, there is a need for the development of new techniques and methods in quantitative remote sensing to address these issues and improve the accuracy and efficiency of data processing and estimation<sup>21,23</sup>.

Deep learning surpasses traditional machine learning methods in data processing capabilities, automated feature learning, and generalization, making it well-suited for handling complex, high-dimensional big data and achieving superior performance in various tasks<sup>21,24</sup>. This paper investigates the feasibility of integrating quantitative remote sensing with computer vision, using generative modeling in deep learning as a case study. We explore how combining these fields can enhance data processing and analysis in quantitative remote sensing.

### The Intersection of Quantitative Remote Sensing and Computer Vision

The widespread adoption of deep learning techniques has enabled the extraction of deep-seated features to their fullest potential, leading to significant improvements in accuracy<sup>10,25,26</sup>.

**Machine learning.** Many current studies have utilized traditional machine learning methods such as Ordinary Least Squares (OLS), Random Forest (RF), and Support Vector Regression (SVR)<sup>21,24,27</sup>. While these methods are straightforward and efficient, their estimation accuracy is often limited. The application of deep learning methods in carbon stock estimation remains relatively unexplored. Deep learning models, particularly generative models, have the ability to generate new samples, enhance data utilization, improve model generalization, and address issues related to insufficient or incomplete data, making them well-suited for carbon stock estimation. Generative models aim to model the distribution of real data by learning from multi-modal data using implicit variable techniques.

**Generative model.** The Generative Adversarial Network (GAN), proposed by Goodfellow et al.<sup>28</sup>, comprises generators and discriminators that engage in adversarial training to produce high-quality samples. However, GAN training can be unstable and prone to mode collapse, requiring careful parameter tuning and attention throughout the training process. Variational Autoencoders (VAE), proposed by Kingma and Welling<sup>29</sup>, enhance sample continuity and controllability by learning a continuous latent space. Despite this, VAEs often underperform compared to GANs in generating high-quality, realistic samples, possibly due to the vagueness inherent in their latent space.

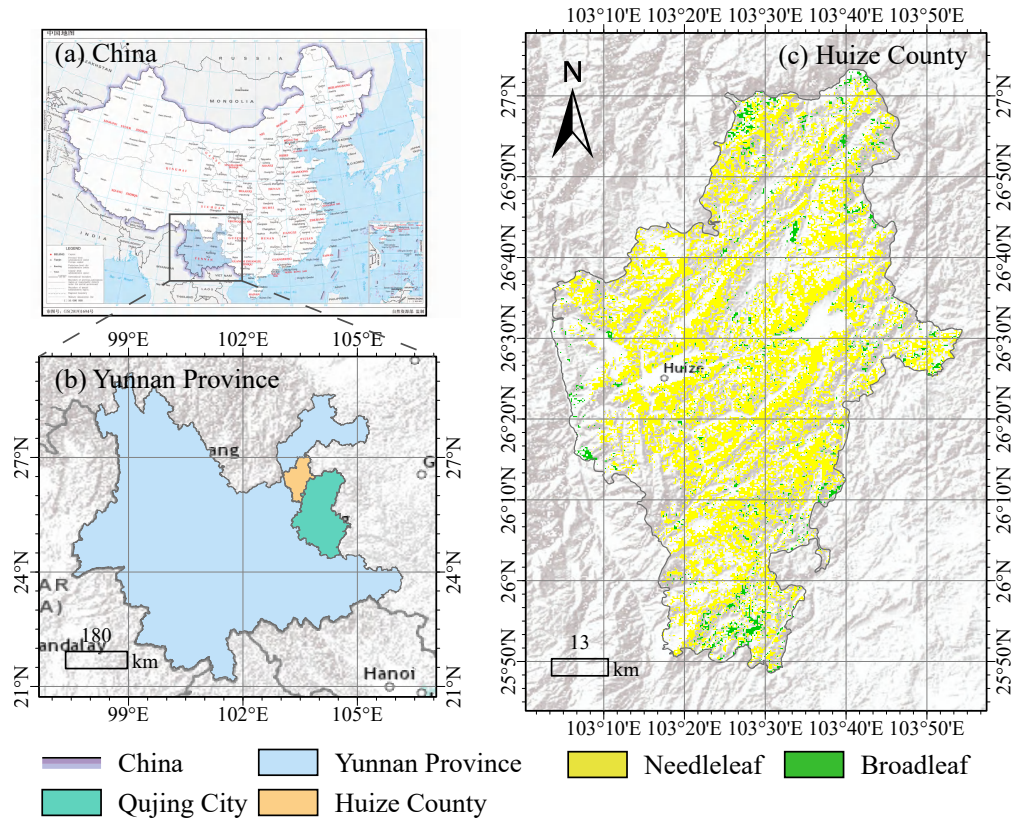


**Figure 1.** Study area. Notes: (a) China, (b) Yunnan Province, and (c) Huize County. The basemap is provided by ArcGIS Pro.

**Diffusion model.** The diffusion model, first introduced in 2015<sup>30</sup>, aims to progressively remove Gaussian noise from training images, functioning similarly to a series of denoising autoencoders. Variants like the Latent Diffusion Model (LDM) train autoencoders to map images into low-dimensional latent spaces. The diffusion model excels in generating high-quality samples with flexibility, stability during training, and resistance to mode collapse, effectively bridging the gaps between GANs and VAEs by combining their strengths. Subsequent models such as DDPM<sup>31</sup>, DDIM<sup>32</sup>, and Stable Diffusion<sup>33</sup> have extended the diffusion model's applications to image generation, consistently achieving state-of-the-art (SOTA) results. These models have been widely applied in image translation tasks. Building on these advancements, we applied the diffusion model structure to estimate carbon stock in remote sensing images, aiming to achieve improved accuracy in this domain.

## Materials

### Study area

Huize County is part of Qujing City, Yunnan Province, China, located at the intersection of Yunnan, Sichuan, and Guizhou Provinces. Covering an area of 5,889 km<sup>2</sup> (Figure 1), Huize features a ladder-shaped terrain with higher peaks in the west and lower valleys in the east. The county experiences a typical temperate plateau monsoon climate, with climates ranging from subtropical in the south to cold temperate in the north. Elevations vary widely, from the highest peak at 4,017 m to the lowest point at 695 m. According to Forest Management Inventory data, Huize County has approximately 3,080.53 km<sup>2</sup> of forest land, with arbor forest land covering approximately 2,538.20 km<sup>2</sup> (82.39%). Rich in forest resources, Huize provides diverse research samples, although its complex landscape poses significant challenges.

### Data sources

**Survey data.** The study utilized 2020 data from the Forest Management Inventory obtained from the Huize County Forestry and Grass Bureau. This comprehensive data includes over 70 attributes such as forest area and type, providing an objective overview of forest resources. It aids in understanding and evaluating the status, trends, distribution, and ecological environment

of forest resources, providing a scientific basis for forestry management, protection, and sustainable utilization.

**Satellite imagery.** The study primarily used GF-1 WFV image data. Launched by China in 2013, the GF-1 satellite provides medium-resolution remote sensing with a spatial resolution of 16 meters. It is widely used in agriculture, forestry, environmental monitoring, and more. For time consistency, images from August 27, 2020, were used for model training, covering the entire study area. Data details are provided in Table A1.

**Elevation data.** The study utilized ALOS PALSAR DEM data with a spatial resolution of 12.5 meters, achieving full coverage of the study area with four-view images (Table A1). ALOS PALSAR, a satellite equipped with a Synthetic Aperture Radar (SAR) sensor, scanned the Earth’s surface with radar beams to measure topographic altitude and surface characteristics. The L-band SAR of PALSAR provided detailed, all-weather interferometric measurements from 2006 to 2011.

**Canopy height.** The study utilized a 10-meter vegetation canopy height dataset from the ETH Global Sentinel-2<sup>34</sup>. Lang et al.<sup>34</sup> fused GEDI and Sentinel-2 data to develop a probabilistic deep learning model for retrieving canopy height from Sentinel-2 imagery globally. The global canopy height map is based on Sentinel-2 images taken between May and September 2020. We extracted the relevant data for Huize County.

## Methods

### Pre-processing

Pre-processing procedures are described in Appendix Section 1. The pre-processing process includes carbon stock & distribution density calculation, and forest/non-forest areas identification.

### Knowledge distillation (KD) module

The Knowledge Distillation (KD) module consists of four parts, and a detailed description is provided in Appendix Section 2.

**Source model.** VGG-19 was selected as an illustrative model for our approach. In this context, the input layer of VGG-19 served as the source model, denoted as *ENC*, from which the knowledge of the features was extracted. Subsequently, this knowledge was transferred to a smaller target model, referred to as *enc*. The architecture of the *enc* model mirrored that of the source model (*ENC*), albeit with a reduced channel length at each layer.

**Global eigenbases.** We adopted a global image-independent eigenbase denoted as  $\mathbf{W}_{N,g} \in \mathbb{R}^{C_N^e \times C_N}$ . In essence, we established a distinctive  $C_N^e$ -dimensional space adept at effectively encapsulating the overarching global features present in the image, as evidenced by Eq. 8.

$$\max_{\mathbf{W}_{N,g}, \mathbf{W}_{N,g}^T = \mathbf{I}} \frac{1}{M} \sum_{k=1}^M \text{tr}(\mathbf{W}_{N,g} \bar{\mathbf{F}}_{N,k} \bar{\mathbf{F}}_{N,k}^T \mathbf{W}_{N,g}^T) \quad (1)$$

**Blockwise PCA-based KD.** To facilitate feature transformation within the distillation model, it was necessary to incorporate a paired decoder denoted as *dec*. This decoder worked in tandem with the encoder *enc* to extract the input information effectively. The distillation method used in this context was Principal Components Analysis (PCA). This module is shown in Fig. 2

**Reducing channel lengths.** In accordance with the empirical principles of PCA dimensionality reduction, it was imperative to preserve the most vital information encapsulated in the channel length  $L_N^e$  of the target model *enc*. Specifically, the target layer *reluN<sub>e</sub>* of  $L_N^e$  should retain variance information exceeding 85% of that found in the source layer *reluN*.

### Denosing model

The conditional network used a Convolutional Neural Network (CNN) to extract conditional features, with the KD-VGG module establishing the initial features  $\mathbf{f}^{(0)}$ . By optimizing KD-VGG, we increased the network depth for deeper feature extraction and significantly reduced the number of parameters, enhancing performance without additional computational overhead.

Subsequently, we concatenated  $\mathbf{f}^{(0)}$  with  $\mathbf{y}_t$  and fed them into the UNet for encoding. Simultaneously, they were downsampled to generate  $\mathbf{f}^{(i)}$ , as illustrated in Eq. 2.

$$\mathbf{f}^{(i)} = \text{Conv}(\mathbf{f}^{(i-1)}) \quad (2)$$

Where, the serial number *i* represented the output of different layers, and *t* was the time. In contrast to GAN-based methodologies, which depend on the incorporation of additional prior knowledge, this conditional network only offers encoded features and transmits them to the UNet, all without the need for additional prior information to model potential representations.

This study constituted an estimation task, in which the dimensions of both the input and output images remained unchanged. In particular, modifications were made to the modulation of the scaling factor (*s*) modulation within the original model. By

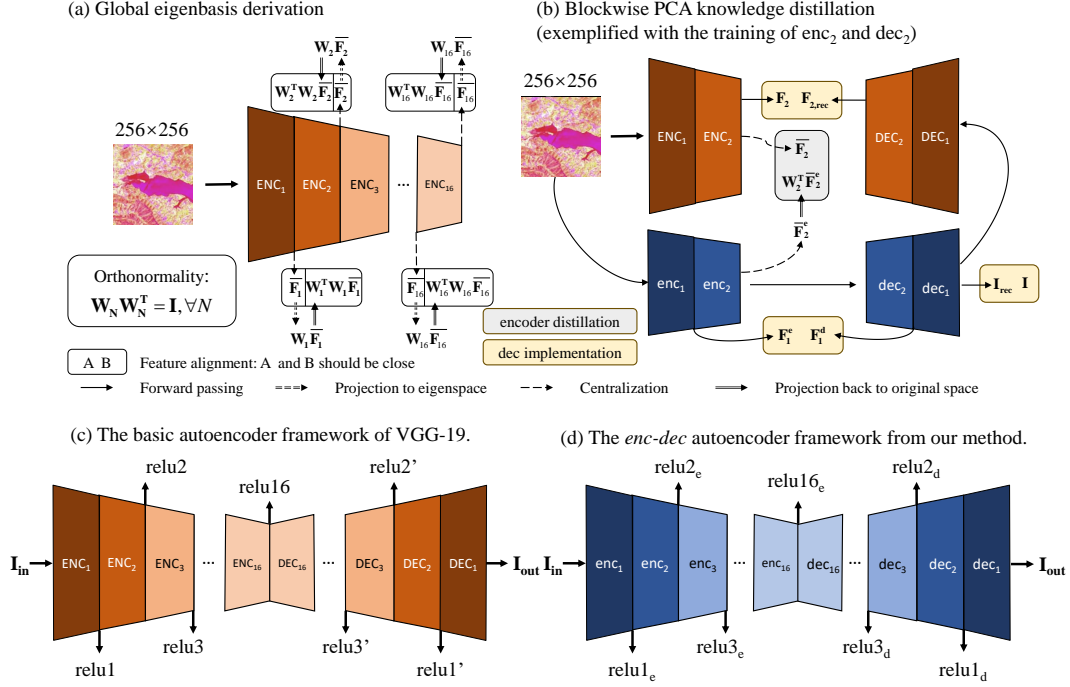


**Figure 2.** PCA-based knowledge distillation structure for VGG. Notes: PCA-based knowledge distillation consists of two steps: (a) global eigenbasis ( $\mathbf{W}_N, N = 1, 2, 3, \dots, 16$ ) derivation, (b) blockwise PCA knowledge distillation, (c) the basic autoencoder framework of VGG-19, and (d) the  $enc-dec$  autoencoder framework from our method.  $relu16_e = relu16'$ , and  $relu16_d = relu16_d$ .

setting this factor to 1, the zoom control for that specific component was eliminated. Building on the foundation of the original model<sup>35</sup>, we introduced attention mechanisms to facilitate the fusion of features derived from  $\mathbf{f}^{(i)}$  and  $\mathbf{u}^{(i)}$ , followed by their input into the implicit representation module.

### Implicit representation

Presently, prevalent algorithms often rely on intricate cascading or two-stage training procedures. However, our research discovered that the use of implicit neural representations for image representation learning notably enhanced estimation accuracy. To implement this, we incorporated several coordinate-based Multi-layer Perceptrons (MLPs) into the up-sampling stage of the UNet architecture, thereby enabling the parameterization of implicit neural representations. We employed a two-layer MLP denoted as  $D$  to perform up-sampling.

$$\mathbf{u}_{up}^{(i)} = D_i(\hat{\mathbf{h}}^{(i+1)}) \quad (3)$$

### Improved implicit diffusion model (IIDM)

The Implicit Diffusion Model (IDM) combined diffusion models and implicit neural representations for image-to-image transformation. The Improved Implicit Diffusion Model (IIDM) workflow is shown in Fig. 3. We used a Recurrent Neural Network (RNN) to create a time-dependent structure with shared parameters, including a denoising and implicit representation model, employing variational inference. Unlike Variational Autoencoders (VAE), the implicit variables in diffusion models have the same dimensionality as the original data, with a predefined and fixed diffusion process.

The Diffusion principle's derivation of forward and reverse processes is shown in Appendix Section 3. The diffusion model included two processes: the diffusion process (that is, the forward process) and the reverse process. Both the forward and reverse processes were a parameterized Markov chain, in which the reverse process can be used to generate data.

The added KD-VGG module can extract the shallow features of  $\mathbf{x}$  and  $\mathbf{y}_t$ , which are then passed into KD-UNet for encoding and decoding to reconstruct the spatial distribution density image. The concatenation of  $\mathbf{f}^0$  and  $\mathbf{y}_t$  enables real-time updating of the model, i.e., updating with the change of  $t$ . Cross-attention effectively handles the relationship between the two features, facilitating their fusion. The multi-layer perceptron (MLP) merges the condition and features, increasing the influence of the condition on the parameters and speeding up the fitting process.

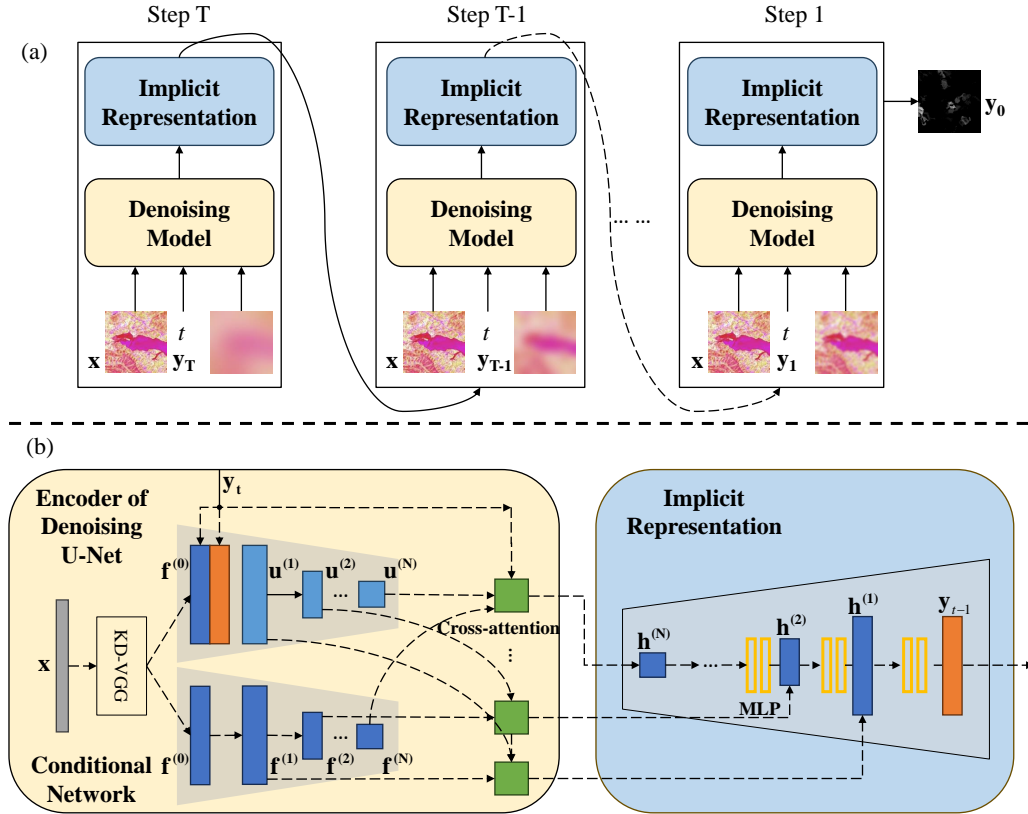


**Figure 3.** Improved implicit diffusion model architecture. Notes: (a) Reverse process of the inference. (b) Denoising model and implicit representation. The denoising model includes KD-VGG feature extractor, encoder of KD-UNet, and conditional network. MLP represents multi-layer perceptron.

### Optimization

The implicit diffusion model aimed to infer the target image  $y_0$  using a series of denoising steps. To achieve this, the denoising model  $\varepsilon_\theta$  was optimized to restore the target image  $y_0$  from a noisy target image  $\tilde{y}_t = \sqrt{\gamma_t}y_0 + \sqrt{1 - \gamma_t}\varepsilon$ . To achieve this, the denoising model  $\varepsilon_\theta$  was optimized to restore the target image  $y_0$  from a noisy target image  $\tilde{y}_t = \sqrt{\gamma_t}y_0 + \sqrt{1 - \gamma_t}\varepsilon$ . Ultimately, the denoising network was optimized to achieve the goal while maintaining the accuracy of the predicted noise  $\varepsilon$ , as shown in Eq. 4.

$$\mathbb{E}_{(x,y)} \mathbb{E}_{\varepsilon,\gamma,t} \|\varepsilon - \varepsilon_\theta(x, t, \tilde{y}_t, \gamma)\|_1^2 \quad (4)$$

where  $\varepsilon \sim \mathcal{N}(0, \mathbf{I})$ ,  $t \sim \{1, \dots, T\}$ , and  $(x, y)$  was sampled from the training set of input-output image pairs.

### Evaluation metrics

Mean Absolute Error (MAE) measures the average absolute error between predicted and actual values. Mean Squared Error (MSE) is the average squared error, and Root Mean Squared Error (RMSE) is the square root of the MSE. Peak Signal-to-Noise Ratio (PSNR) and Structural Similarity Index Metric (SSIM) are full-reference image quality indices, with PSNR assessing overall image quality and SSIM evaluating similarity in brightness, contrast, and structure.

## Results

### Inference time

We used  $256 \times 256$  images, and the test results included seven models (as shown in Appendix Table A3): VGG, KD-VGG, Stable Diffusion (SD), DDPM, DDIM, Ours-VGG, and Ours-KD-VGG. DDPM, DDIM, and SD were diffusion models with more than 450M parameters. Adding modules for improved accuracy could lead to high system overhead and reduced feasibility, prompting a discussion on the justification for such additions.

The VGG-19 model, originally with 76.39M parameters, was reduced to 0.99M parameters after dimensionality reduction, achieving approximately 77 times compression. The KD-VGG-19 model retained most of VGG-19's feature extraction capabilities while significantly reducing its size, making it a lightweight and efficient feature extraction module for downstream tasks. Similar compression methods were applied to VGG-16 and VGG-11, achieving compression ratios of 89.49 and 184.80 times, respectively. Among the three, VGG-11 had the highest compression efficiency, followed by VGG-16, while VGG-19, though least compressed, performed best in estimation.

The VGG module was incorporated into the feature extraction section of IDM. KD-VGG maintained the model's robust feature extraction capabilities and improved estimation accuracy while reducing inference time with scaled-down parameters. The inference times for KD-VGG-11, KD-VGG-16, and KD-VGG-19 were 97.22%, 86.22%, and 89.97% of their pre-KD times, respectively, while the inference time of KD-UNet was 61.92% of the original UNet. UNet compression had a more significant impact on inference time compared to VGG. The IDM parameters were only about 9% of the SD's, with 11.28M more than DDPM. Our VGG model required 72.80~73.60M fewer parameters than IDM, accounting for just ~7.5% of SD. DDPM had the fastest inference time among the diffusion models, and our VGG model was even faster than IDM by 0.17~0.18 seconds. The reduction in model parameters enables easy deployment in common devices and the reduced inference time facilitates the application of large models to quantitative remote sensing with substantial data volumes.

## Model compression

### ***KD-VGG.***

During the distillation process, principal components with a cumulative contribution rate higher than 85% were selected to maximize effective information extraction unsupervisedly. This enabled channel dimensionality reduction, decreasing model parameters. VGG initially presented an increasing channel length, which was reduced after dimensionality reduction. This indicated that deeper layers had more invalid channels, and reducing these channels effectively decreased parameters with minimal impact on accuracy. This is likely because most effective features are extracted in the middle layers, while deeper layers do not require such complexity. VGG-11, VGG-16, and VGG-19 all showed improved performance with deeper layers. For example, VGG-19's distillation results are shown in Table A2, and the dimensionality reduction results for 16 features are depicted in Figure 4.

### ***KD-UNet.***

PCA performed dimensionality reduction based on feature transformations and spatial mapping, while PCA-based distillation was interpretable and generalizable and can be used for model compression of other network structures. IDM contained the UNet structure, and we applied this to the UNet with a view to maximize the compression of diffusion models. The distillation results are shown in Appendix Table A2, and the channel downscaling results for the 10 features are shown in Appendix Fig. A1. UNet was a *enc-dec* structure and requires a skip connection, which required the same number of channels in the front and back structure. Moreover, there existed an upsample between each 2 layers, so it was necessary to present a double number of channels. We added Selected column in Appendix Table A2 to describe the final number of selected channels. The selection was based on the minimum channel length that meets the requirements, and the final selection was (44, 44, 88, 88, 176, 176, 352, 352, 704, 704).

## Ablation study

Five modules were selected for the ablation experiment: Mask, VGG, KD-VGG, KD-UNet and Attention + MLP, detailed in Table 1. Mask filtered vegetation and non-vegetation areas effectively, serving as the initial data preprocessing stage. VGG and KD-VGG modules were employed for the initial extraction of features, with a comparable performance observed between KD-VGG and VGG models. However, VGG slightly outperformed KD-VGG, highlighting the effectiveness of knowledge distillation in extracting critical model parameters while indicating areas for further enhancement. Introducing attention and MLP modules resulted in improved model performance, albeit with increased computational influence time. The results indicated a significant accuracy enhancement after the integration of the modules, confirming the optimization achieved through the joint use of the KD-VGG and Attention + MLP modules. Thus, the strategy of prioritizing accuracy over computational time proved beneficial.

## Comparison of different models

We selected seven comparison models, including commonly used regression models in remote sensing estimation (OLS, RF, and SVR), and deep learning generative models (VAE, GAN, and IIDM proposed in this paper). The results are presented in Table 2. OLS was the simplest and least computationally expensive algorithm among all models. RF and SVR were the most widely used machine learning algorithms for estimation. However, the accuracy of these three algorithms was similar and generally poor in all models. The accuracy of deep learning algorithms was significantly better, with generative models outperforming VAE and diffusion models outperforming GAN. Among all models, IDM-VGG achieved the best performance,

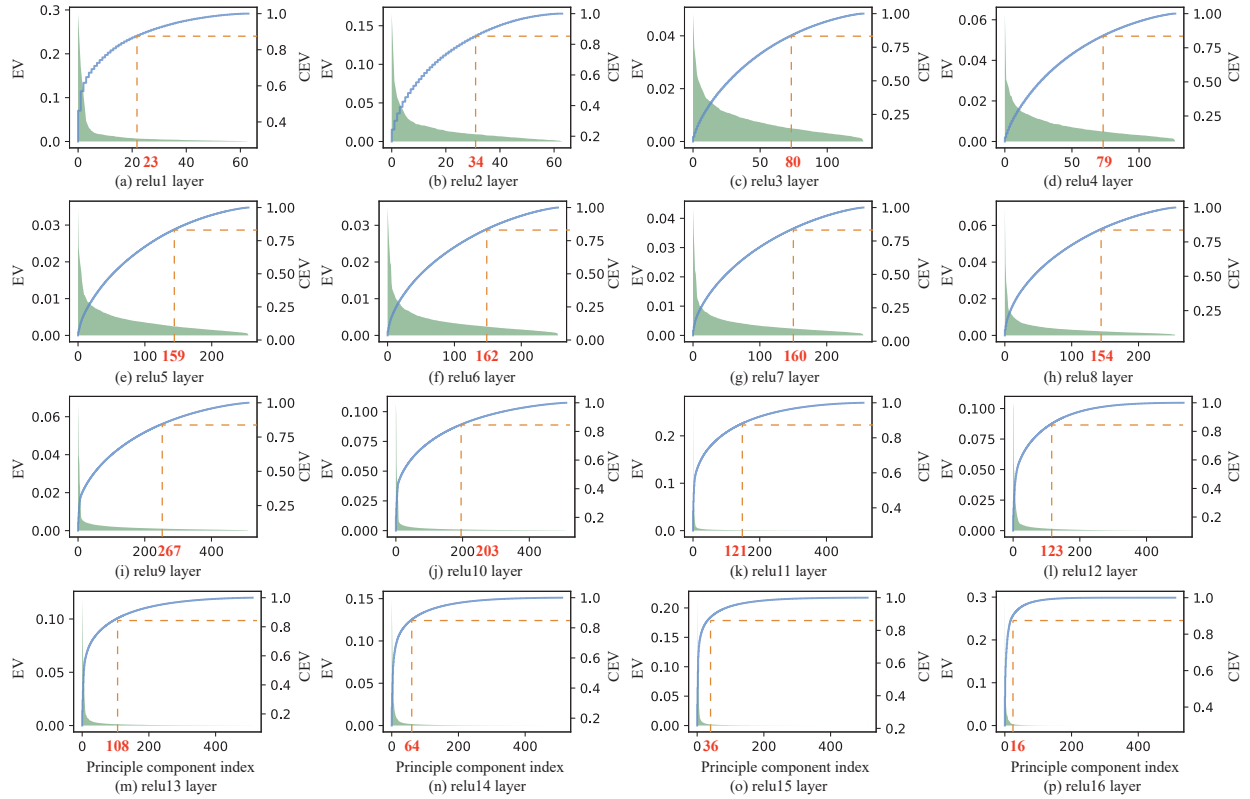


**Figure 4.** Features of VGG. Notes: Take VGG-19 as an example. Mean explained variance (green area) and mean cumulative explained variance (blue curve) of the  $relu_N$  features.

**Table 1.** Compare of modules, including Mask, VGG, KD-VGG, and Attention + MLP. Notes: We choose VGG-19 and KD-VGG-19. Bold is the best, and underline is the second. KD-V = KD-VGG, KD-U = KD-UNet, and A+MLP = Attention + MLP.

No.	Mask	VGG	KD-V	KD-U	A+MLP	MAE↓	RMSE↓	SSIM↑	PSNR↑
1	×	✓	×	×	×	0.0965	0.1670	0.5986	19.0697
2	×	✓	×	✓	×	0.0924	0.1697	0.6098	18.9279
3	×	✓	×	✓	✓	0.0921	0.1680	0.6357	19.0166
4	×	×	✓	✓	×	0.0924	0.1692	0.6073	18.9546
5	×	×	✓	✓	✓	0.0925	0.1684	0.6192	18.9969
6	×	×	×	✓	✓	0.0959	0.1670	0.5879	19.0662
7	✓	✓	×	×	×	0.0742	0.1363	0.7283	20.8318
8	✓	✓	×	✓	×	0.0692	0.1229	0.7196	21.7321
9	✓	✓	×	✓	✓	<b>0.0687</b>	<b>0.1211</b>	<u>0.7289</u>	<b>21.8581</b>
10	✓	×	✓	✓	×	0.0691	0.1288	<b>0.7388</b>	21.4396
11	✓	×	✓	✓	✓	<u>0.0688</u>	<u>0.1217</u>	0.7186	<u>21.8167</u>
12	✓	×	×	✓	✓	0.0702	0.1306	0.7207	21.2021



**Table 2.** Compare of carbon stock estimation. Notes: The following results have all added masks. OLS = Ordinary Least Squares, RF = Random Forest, SVR = Support Vector Regress, VAE = Variational Autoencoder, and GAN = Generative Adversarial Network. Bold is the best, and underline is the second.

Model	MAE↓	RMSE↓	SSIM↑	PSNR↑
OLS	0.5352	0.5450	0.3619	8.7943
RF	0.5272	0.5386	0.3722	8.8963
SVR	0.5117	0.5233	0.3365	9.1475
VAE	0.3036	0.3770	0.3514	11.8163
GAN	0.2577	0.2942	0.4089	14.1501
IDM-VGG-11	0.1061	0.1797	0.6649	18.4298
IDM-KD-VGG-11	0.1064	0.1814	0.6682	18.3499
IDM-VGG-16	0.0955	0.1769	0.6639	18.5664
IDM-KD-VGG-16	0.0959	0.1794	0.6665	18.4433
IDM-VGG-19	0.0862	0.1732	0.6573	18.7506
IDM-KD-VGG-19	0.0868	0.1766	0.6817	18.5803
IDM-UNet	0.0761	0.1500	0.7024	20.0000
IDM-KD-UNet	0.0788	0.1513	0.6953	19.9235
Ours-KD-VGG-11	0.0721	0.1389	0.7149	20.6663
Ours-KD-VGG-16	<u>0.0709</u>	<u>0.1367</u>	<u>0.7163</u>	<u>20.8034</u>
Ours-KD-VGG-19	<b>0.0688</b>	<b>0.1217</b>	<b>0.7186</b>	<b>21.8167</b>

followed closely by IDM-KD-VGG (IIDM), with only a slight difference in accuracy between the two. Taking into account both the parameters and the inference time, IIDM proved to be more versatile.

The spatial distribution results, illustrated in Figure 5, revealed different patterns. The distributions generated by the OLS, RF, and SVR algorithms showed significant deviations from the ground truth. Generally, these three algorithms consistently overestimated the values, with RF producing the highest estimates, followed by OLS. Although estimates for high-value regions were relatively close to the actual values, the overall discrepancies were substantial. Both RF and SVR exhibited noticeable point noise, indicating instability in their estimation results.

Conversely, the estimations from VAE, GAN, and IIDM closely approximated the ground truth. VAE showed more pronounced low-value regions, whereas GAN consistently produced higher estimates. IIDM demonstrated high detail fidelity, closely aligning with the ground truth, though its performance in extreme value regions was not as robust as that of GAN.

### Applied to other study areas

We applied this model to the region of Yunnan Province and estimated the density of carbon stock distribution in February / May / August / November 2020, as shown in Fig 6. Since Yunnan Province is located in the plateau region, the meteorological characteristics of cloudy and rainy conditions lead to limited available images, so the estimation was only achieved for four time points.

The carbon stock distribution density in Yunnan Province showed significant spatial and temporal variations throughout the year, with notable areas of increase and decrease. This analysis provides insights into these changes. The northwest part of Yunnan Province exhibits high values throughout the year, while the central part shows low values. In the northeast, higher values are observed in spring and summer, whereas low values are seen in fall and winter. As the temperature decreases, the region of high values tends to shift towards the southwest.

In conclusion, the distribution of the density of the carbon stock in Yunnan Province in 2020 reveals spatial and temporal variations with seasons, proving the feasibility of the model for large-area observations. At the same time, these findings emphasize the importance of continued forest management and conservation efforts to maintain and enhance the ecological and socio-economic benefits of the region's forests.

## Discussion

### Simplify temporal and spatial complexity

PCA, a widely used data transformation method, primarily focuses on dimensionality reduction by identifying principal components. It transforms original data into a new coordinate system, preserving variance while reducing dimensionality. PCA

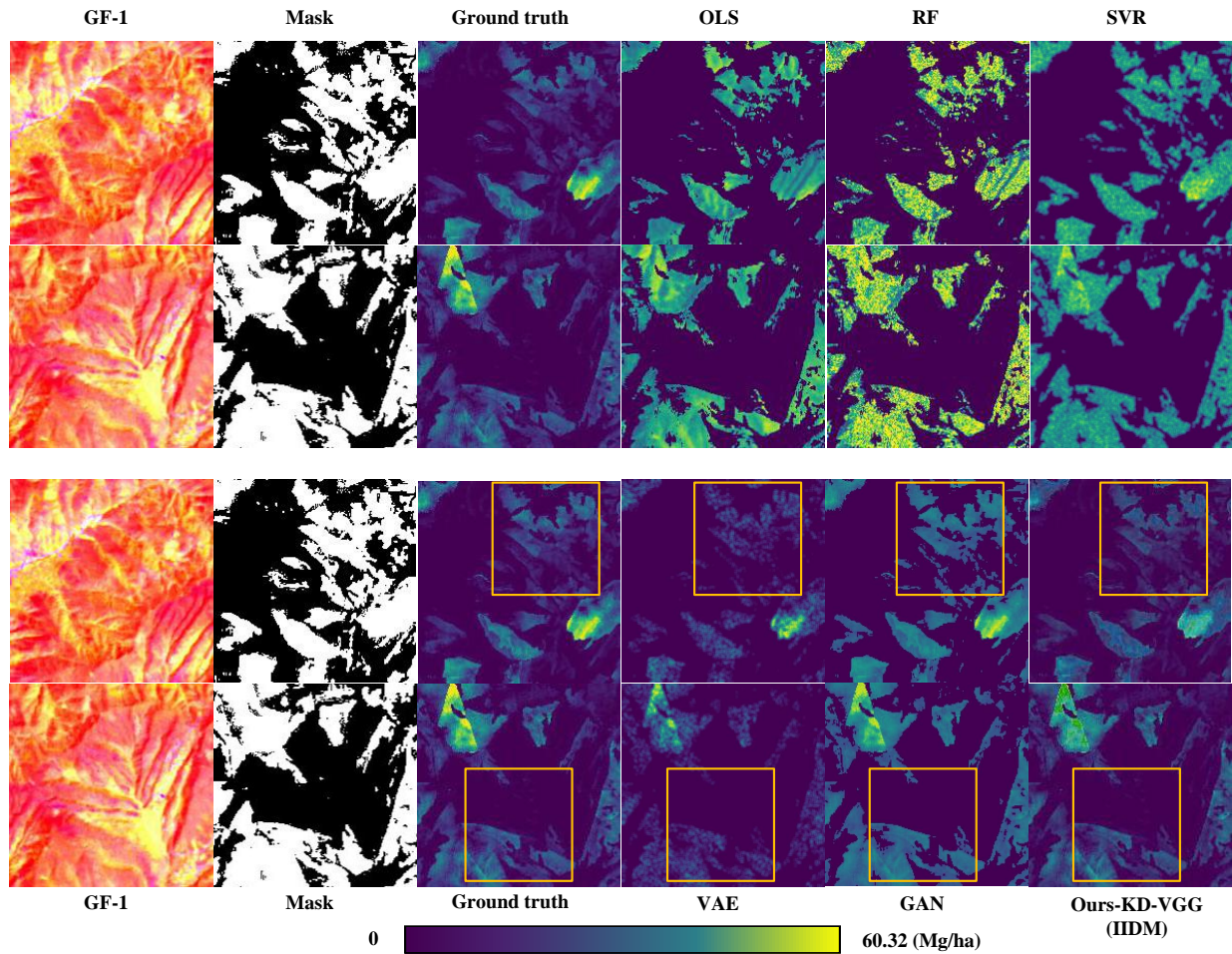


**Figure 5.** Carbon stock estimation results. Notes: The above results have all added masks. OLS = Ordinary Least Squares, RF = Random Forest, SVR = Support Vector Regress, VAE = Variational Autoencoder, and GAN = Generative Adversarial Network.

maps high-dimensional data to lower dimensions, retaining significant variance. This technique is used in feature selection, data compression, noise mitigation, and data visualization<sup>36–39</sup>.

The advantages of PCA include simplicity, efficiency, and ease of implementation. It reduces data complexity, improves computational efficiency, removes redundant information, and identifies critical features and patterns. Its high interpretability and generalizability make it a versatile tool for model compression across various network architectures.

### Comparison of estimation models

Carbon stock estimation posed a regression challenge, with several modeling approaches considered for the task. **Ordinary Least Squares (OLS):** Simple and interpretable with clear parameter estimation, but vulnerable to outliers, underfitting, and poor performance on complex nonlinear problems<sup>40</sup>. **Random Forest (RF):** Resistant to overfitting, effective with high-dimensional data and many features, but lacks explicit parameter estimates and interpretability<sup>41</sup>. **Support Vector Regression (SVR):** Handles complex data relationships well, is robust to outliers, but highly dependent on parameter selection and has limited interpretability<sup>42</sup>. **Generative Adversarial Network (GAN):** Generates realistic samples, but training is unstable and results lack diversity and interpretability<sup>43</sup>. **Variational Autoencoder (VAE):** Learns variable representations and probability distributions with strong interpretability and diverse samples, but reconstructed results can be fuzzy<sup>44</sup>. **Diffusion Models:** Generate high-quality samples with controllable diversity, suitable for multimodal data, but require significant computational resources and longer training times<sup>45</sup>. This study highlights the potential of AIGC in quantitative remote sensing research, providing insights into the selection and application of various modeling techniques.

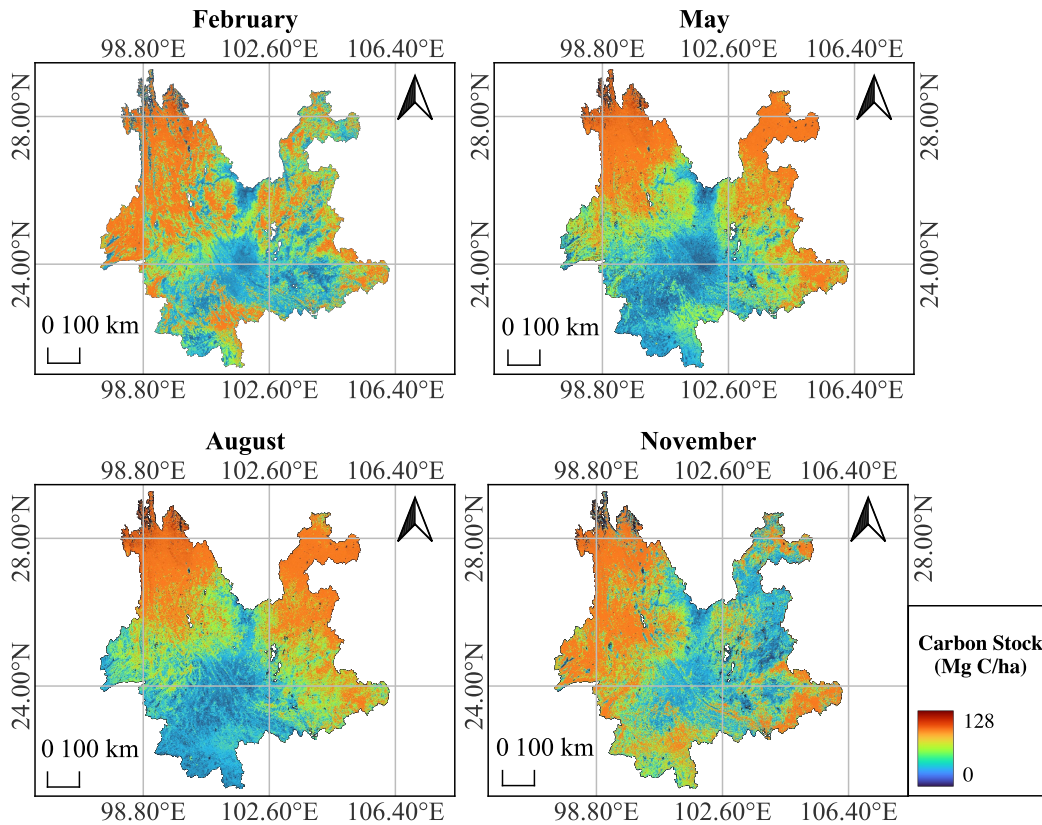


**Figure 6.** Carbon stock temporal and spatial variation characteristics in 2020.

### Comparison with existing products

The abundant forest resources provide a solid research foundation, but its varied altitude complicates precise carbon stock calculations. Current estimation methods using satellite imagery are divided into optical imagery and LiDAR. Although LiDAR offers high accuracy, it faces challenges in large-scale applications and data acquisition. Optical imagery, particularly from GF-1, overcomes these issues, making high-precision carbon stock estimation a key research challenge.

Traditional multi-spectral carbon stock estimation has relied on machine learning models like OLS, RF, and SVR, which mainly extract linear and shallow nonlinear features. The complex relationship between spectral/textural features and biomass/carbon stock is nonlinear. To address this, we introduced the IIDM algorithm, which extracts deeper features using a deep learning diffusion model, integrating VGG for initial feature extraction, Attention + MLP for feature fusion, and a Mask for non-vegetation area filtering.

The IIDM model significantly improved the estimation accuracy (RMSE = 12.17 Mg/ha), outperforming the LiDAR-based methods (RMSE = 25.64 Mg/ha) and multisource coarse resolution imagery-based methods (RMSE $\approx$ 30 Mg/ha)<sup>46,47</sup>. These results highlight the effectiveness of artificial intelligence generated content (AIGC) in remote sensing image-based land surface parameter estimation.

### Conclusion

Our study focused on Huize County, using GF-1 WFV images and a deep learning generative diffusion model enhanced by knowledge distillation. This approach integrated the VGG module for initial feature extraction, followed by cross-attention + MLPs for feature fusion, and a mask to filter non-vegetated areas, resulting in the IIDM model for accurate regional carbon sink estimation. Key findings include:

- **Knowledge Distillation-Based Module:** By incorporating VGG-19 into the diffusion model for initial feature extraction, the IIDM model reduced inference time, increased accuracy, and minimized model parameters.
- **Feature Fusion with Cross-Attention + MLP:** This method improved carbon stock estimation accuracy by establishing relationships between global and local features, with only a slight increase in inference time, which remained shorter than other diffusion models.

- **Generative Model's Effectiveness:** The generative model excelled in extracting deeper features, significantly outperforming other models. IIDM achieved the highest accuracy in carbon stock estimation with an RMSE of 12.17 Mg/ha, representing a 41.69%~42.33% improvement over regression models.

## Acknowledgments

Thank Prof. Jinnian Wang of Guangzhou University for data support.

## References

1. Lenoir, J. *et al.* Species better track climate warming in the oceans than on land. *Nat. ecology & evolution* **4**, 1044–1059 (2020).
2. Pecchi, M. *et al.* Species distribution modelling to support forest management. a literature review. *Ecol. Model.* **411**, 108817 (2019).
3. Brando, P. M. *et al.* Droughts, wildfires, and forest carbon cycling: A pantropical synthesis. *Annu. Rev. Earth Planet. Sci.* **47**, 555–581 (2019).
4. Nolan, C. J., Field, C. B. & Mach, K. J. Constraints and enablers for increasing carbon storage in the terrestrial biosphere. *Nat. Rev. Earth & Environ.* **2**, 436–446 (2021).
5. Hua, F. *et al.* The biodiversity and ecosystem service contributions and trade-offs of forest restoration approaches. *Science* **376**, 839–844 (2022).
6. Hurtt, G. *et al.* Beyond mrv: high-resolution forest carbon modeling for climate mitigation planning over maryland, usa. *Environ. Res. Lett.* **14**, 045013 (2019).
7. Sun, W. & Liu, X. Review on carbon storage estimation of forest ecosystem and applications in china. *For. Ecosyst.* **7**, 1–14 (2020).
8. Lee, J. *et al.* The first national scale evaluation of organic carbon stocks and sequestration rates of coastal sediments along the west sea, south sea, and east sea of south korea. *Sci. Total. Environ.* **793**, 148568 (2021).
9. Santoro, M., Cartus, O. & Fransson, J. E. Dynamics of the swedish forest carbon pool between 2010 and 2015 estimated from satellite l-band sar observations. *Remote. Sens. Environ.* **270**, 112846 (2022).
10. Xiao, J. *et al.* Remote sensing of the terrestrial carbon cycle: A review of advances over 50 years. *Remote. Sens. Environ.* **233**, 111383 (2019).
11. Gao, F. *et al.* Spatially explicit carbon emissions by remote sensing and social sensing. *Environ. Res.* **221**, 115257 (2023).
12. Long, D. A. *et al.* High-accuracy near-infrared carbon dioxide intensity measurements to support remote sensing. *Geophys. Res. Lett.* **47**, e2019GL086344 (2020).
13. Gray, A. *et al.* Remote sensing reveals antarctic green snow algae as important terrestrial carbon sink. *Nat. Commun.* **11**, 2527 (2020).
14. Chen, Y., Guerschman, J. P., Cheng, Z. & Guo, L. Remote sensing for vegetation monitoring in carbon capture storage regions: A review. *Appl. energy* **240**, 312–326 (2019).
15. He, X. *et al.* Soil organic carbon prediction using phenological parameters and remote sensing variables generated from sentinel-2 images. *Catena* **205**, 105442 (2021).
16. Odebiri, O., Odindi, J. & Mutanga, O. Basic and deep learning models in remote sensing of soil organic carbon estimation: A brief review. *Int. J. Appl. Earth Obs. Geoinformation* **102**, 102389 (2021).
17. Wang, S. *et al.* Using soil library hyperspectral reflectance and machine learning to predict soil organic carbon: Assessing potential of airborne and spaceborne optical soil sensing. *Remote. Sens. Environ.* **271**, 112914 (2022).
18. Puliti, S. *et al.* Above-ground biomass change estimation using national forest inventory data with sentinel-2 and landsat. *Remote. sensing environment* **265**, 112644 (2021).
19. Zhang, Y., Sui, B., Shen, H. & Ouyang, L. Mapping stocks of soil total nitrogen using remote sensing data: A comparison of random forest models with different predictors. *Comput. Electron. Agric.* **160**, 23–30 (2019).
20. Chopping, M., Wang, Z., Schaaf, C., Bull, M. A. & Duchesne, R. R. Forest aboveground biomass in the southwestern united states from a misr multi-angle index, 2000–2015. *Remote. Sens. Environ.* **275**, 112964 (2022).

21. Han, W. *et al.* A survey of machine learning and deep learning in remote sensing of geological environment: Challenges, advances, and opportunities. *ISPRS J. Photogramm. Remote. Sens.* **202**, 87–113 (2023).
22. Yasir, M. *et al.* Coupling of deep learning and remote sensing: A comprehensive systematic literature review. *Int. J. Remote. Sens.* **44**, 157–193 (2023).
23. Pal, S. K., Kumar, D. A. & Meher, S. K. Gri-cnn: Granulated deep learning model with interpretable architecture for remote sensing image classification. *IEEE Transactions on Geosci. Remote. Sens.* (2024).
24. Wang, Z., Ma, Y. & Zhang, Y. Review of pixel-level remote sensing image fusion based on deep learning. *Inf. Fusion* **90**, 36–58 (2023).
25. Matinfar, H. R., Maghsodi, Z., Mousavi, S. R. & Rahmani, A. Evaluation and prediction of topsoil organic carbon using machine learning and hybrid models at a field-scale. *Catena* **202**, 105258 (2021).
26. Pham, T. D. *et al.* Advances in earth observation and machine learning for quantifying blue carbon. *Earth-Science Rev.* 104501 (2023).
27. Li, J., Cai, Y., Li, Q., Kou, M. & Zhang, T. A review of remote sensing image segmentation by deep learning methods. *Int. J. Digit. Earth* **17**, 2328827 (2024).
28. Goodfellow, I. *et al.* Generative adversarial nets. *Adv. neural information processing systems* **27** (2014).
29. Kingma, D. P. & Welling, M. Auto-encoding variational bayes. *arXiv preprint arXiv:1312.6114* (2013).
30. Sohl-Dickstein, J., Weiss, E., Maheswaranathan, N. & Ganguli, S. Deep unsupervised learning using nonequilibrium thermodynamics. In *International conference on machine learning*, 2256–2265 (PMLR, 2015).
31. Ho, J., Jain, A. & Abbeel, P. Denoising diffusion probabilistic models. *Adv. neural information processing systems* **33**, 6840–6851 (2020).
32. Song, J., Meng, C. & Ermon, S. Denoising diffusion implicit models. *arXiv preprint arXiv:2010.02502* (2020).
33. Rombach, R., Blattmann, A., Lorenz, D., Esser, P. & Ommer, B. High-resolution image synthesis with latent diffusion models. In *Proceedings of the IEEE/CVF conference on computer vision and pattern recognition*, 10684–10695 (2022).
34. Lang, N., Jetz, W., Schindler, K. & Wegner, J. D. A high-resolution canopy height model of the earth. *arXiv preprint arXiv:2204.08322* (2022).
35. Gao, S. *et al.* Implicit diffusion models for continuous super-resolution. In *Proceedings of the IEEE/CVF Conference on Computer Vision and Pattern Recognition*, 10021–10030 (2023).
36. Anowar, F., Sadaoui, S. & Selim, B. Conceptual and empirical comparison of dimensionality reduction algorithms (pca, kpca, lda, mds, svd, lle, isomap, le, ica, t-sne). *Comput. Sci. Rev.* **40**, 100378 (2021).
37. Salo, F., Nassif, A. B. & Essex, A. Dimensionality reduction with ig-pca and ensemble classifier for network intrusion detection. *Comput. networks* **148**, 164–175 (2019).
38. Reddy, G. T. *et al.* Analysis of dimensionality reduction techniques on big data. *Ieee Access* **8**, 54776–54788 (2020).
39. Chiu, T.-Y. & Gurari, D. Pca-based knowledge distillation towards lightweight and content-style balanced photorealistic style transfer models. In *Proceedings of the IEEE/CVF conference on computer vision and pattern recognition*, 7844–7853 (2022).
40. Venter, Z. S., Brousse, O., Esau, I. & Meier, F. Hyperlocal mapping of urban air temperature using remote sensing and crowdsourced weather data. *Remote. Sens. Environ.* **242**, 111791 (2020).
41. Sakamoto, T. Incorporating environmental variables into a modis-based crop yield estimation method for united states corn and soybeans through the use of a random forest regression algorithm. *ISPRS J. Photogramm. Remote. Sens.* **160**, 208–228 (2020).
42. Zhang, Y. *et al.* Improving remote sensing estimation of secchi disk depth for global lakes and reservoirs using machine learning methods. *GIScience & Remote. Sens.* **59**, 1367–1383 (2022).
43. Li, X., Du, Z., Huang, Y. & Tan, Z. A deep translation (gan) based change detection network for optical and sar remote sensing images. *ISPRS J. Photogramm. Remote. Sens.* **179**, 14–34 (2021).
44. Du, L. *et al.* Two-stream deep fusion network based on vae and cnn for synthetic aperture radar target recognition. *Remote. Sens.* **13**, 4021 (2021).
45. Yang, L. *et al.* Diffusion models: A comprehensive survey of methods and applications. *arXiv preprint arXiv:2209.00796* (2022).

46. Cao, L. *et al.* Estimation of forest biomass dynamics in subtropical forests using multi-temporal airborne lidar data. *Remote. Sens. Environ.* **178**, 158–171 (2016).
47. Chen, Y. *et al.* Maps with 1 km resolution reveal increases in above-and belowground forest biomass carbon pools in china over the past 20 years. *Earth Syst. Sci. Data* **15**, 897–910 (2023).
48. Yu, Z., Wang, J., Yang, X. & Ma, J. Superpixel-based style transfer method for single-temporal remote sensing image identification in forest type groups. *Remote. Sens.* **15**, 3875 (2023).

## Supplementary Material

### Pre-processing

**Calculate carbon stock.** The survey data did not include carbon stock, but the accumulation data per hectare was included. The calculation of forest carbon stock is shown in Eq. 5. The default values of conversion factors for climate change projections were used for the Intergovernmental Panel on Climate Change (IPCC). The volume expansion coefficient  $\delta$  was generally taken as 1.90, and the bulk density coefficient, that is, the dry weight coefficient,  $\rho$ , was generally taken as 0.45~0.50 t/m<sup>3</sup>. In this study, we used 0.5 t/m<sup>3</sup>. The carbon content rate  $\gamma$  was generally taken as 0.5,  $V$  was the accumulated volume (m<sup>3</sup>), and  $C$  was the carbon stock (t or Mg). The accumulated volume was calculated as shown in Eq. 6, where  $V_{ha}$  was the volume per hectare (m<sup>3</sup>/ha) and  $Area$  was the plaque area (ha).

$$C = 2.439 \times (\delta \times \rho \times \gamma \times V) \quad (5)$$

$$V = V_{ha} \times Area. \quad (6)$$

**Calculate distribution density.** We used the plaque of survey data as a unit area, normalized the canopy height within the area as the weight, and calculated the carbon stock density as shown in Eq. 7. Where,  $i$  was the area number,  $C$  was the carbon stock,  $W$  was the weight,  $CD$  was the carbon stock of each pixel, i.e. the carbon stock density.

$$CD_i = C_i \times W_i \quad (7)$$

**Identify forest/non-forest areas.** On the basis of previous research, we selected F-Pix2Pix proposed by Yu et al.<sup>48</sup> to extract the forest area, considered it as a mask, and binarized the extracted image. The forest area was designated as 255, and the non-forest area was set to 0.

**Table A1.** Data information.

Name	Abbreviation	Format	Date	Resolution	Product ID/Source
GF-1 WFV	GF-1	GeoTIFF	2020/8/27	16 m	GF1_WFV3_E103.7_N25.6_20200827_L1A0005020371
GF-1 WFV	GF-1	GeoTIFF	2020/8/27	16 m	GF1_WFV3_E104.2_N27.3_20200827_L1A0005020368
ALOS PALSAR DEM	DEM	GeoTIFF	2006~2011	12.5 m	AP_24748_FBD_F0520_RT1.dem.tif
ALOS PALSAR DEM	DEM	GeoTIFF	2006~2011	12.5 m	AP_24748_FBD_F0510_RT1.dem.tif
ALOS PALSAR DEM	DEM	GeoTIFF	2006~2011	12.5 m	AP_24748_FBD_F0500_RT1.dem.tif
ALOS PALSAR DEM	DEM	GeoTIFF	2006~2011	12.5 m	AP_19132_FBD_F0510_RT1.dem.tif
Global Canopy Height 2020	Canopy Height	GeoTIFF	2020	10 m	-
Forest Resource Management Inventory Data	-	Shapefile	2020	-	Forestry and Grassland Bureau of Huize County

### Knowledge distillation (KD) module

**Source model.** VGG-19 was selected as an illustrative model for our approach. In this context, the input layer of VGG-19 served as the source model, denoted as  $ENC$ , from which feature knowledge was extracted. Subsequently, this knowledge was transferred to a smaller target model, referred to as  $enc$ . The architecture of the  $enc$  model mirrored that of the source model ( $ENC$ ), albeit with a reduced channel length at each layer.

The knowledge of features extracted from the  $reluN$  ( $N = 1, 2, 3, \dots, 16$ ) layer of  $ENC$  was mapped to the corresponding layer in  $enc$ , referred to as  $reluN_e$  layer. Concretely,  $\mathbf{F}_{N,k}$  represented the features extracted from the image  $I_k$  at the  $reluN$  layer of  $ENC$ , such that  $\mathbf{F}_{N,k} \in C_N \times H_{N,k} W_{N,k}$ . On the other hand,  $\mathbf{F}_{N,k}^e$  denoted the features extracted at the corresponding  $reluN_e$  layer of  $enc$ , with dimensions  $\mathbf{F}_{N,k}^e \in C_N^e \times H_{N,k} W_{N,k}$ , where  $C_N^e \ll C_N$ .

**Global eigenbases.** We adopted a global, image-independent eigenbasis denoted as  $\mathbf{W}_{N,g} \in \mathbb{R}^{C_N^e \times C_N}$ . In essence, we established a distinctive  $C_N^e$ -dimensional space adept at effectively encapsulating the overarching global features present in the image, as evidenced by Eq. 8.

$$\max_{\mathbf{W}_{N,g} \mathbf{W}_{N,g}^T = \mathbf{I}} \frac{1}{M} \sum_{k=1}^M \text{tr}(\mathbf{W}_{N,g} \bar{\mathbf{F}}_{N,k} \bar{\mathbf{F}}_{N,k}^T \mathbf{W}_{N,g}^T) \quad (8)$$

**Table A2.** Knowledge distillation results. Notes: Channels: CHNs; mCEV: channels of mCEV > 85.

No.	VGG-19		VGG-16		VGG-11		UNet		
	CHNs	mCEV	CHNs	mCEV	CHNs	mCEV	CHNs	mCEV	Selected
1	64	23	64	24	64	30	64	5	44
2	64	34	64	38	128	80	64	37	44
3	128	80	128	86	256	166	128	65	88
4	128	79	128	87	256	162	128	82	88
5	256	159	256	170	512	250	256	142	176
6	256	162	256	173	512	133	256	167	176
7	256	160	256	158	512	57	512	286	352
8	256	154	512	239	-	-	512	335	352
9	512	267	512	150	-	-	1024	524	704
10	512	203	512	76	-	-	1024	621	704
11	512	121	512	42	-	-	-	-	-
12	512	123	512	13	-	-	-	-	-
13	512	108	-	-	-	-	-	-	-
14	512	64	-	-	-	-	-	-	-
15	512	36	-	-	-	-	-	-	-
16	512	16	-	-	-	-	-	-	-

Where  $M$  was the number of images, and the solution of  $\mathbf{W}_{N,g}$  was the eigenbases of  $\frac{1}{M} \sum_{k=1}^M \bar{\mathbf{F}}_{N,k} \bar{\mathbf{F}}_{N,k}^T$ . Use mini-batch gradient descent to minimize the loss  $\sum_{I_k \in \beta_t} \text{tr}(\mathbf{W}_{N,g} \bar{\mathbf{F}}_{N,k} \bar{\mathbf{F}}_{N,k}^T \mathbf{W}_{N,g}^T) / |\beta_t|$ , where  $\beta_t$  was a batch of sampled images at the  $t^{\text{th}}$  iteration of the gradient descent. The use of the negative trace as a loss function introduced instability into the gradient descent process. These loss functions lacked a lower bound, causing gradient descent algorithms to prioritize minimizing losses while neglecting the constraint  $\mathbf{W}_{N,g} \mathbf{W}_{N,g}^T = \mathbf{I}$ . This was unsolvable in the current situation, and we used Eq. 8 rewriting as Eq. 9 to solve and optimize the problem of  $\mathbf{W}_{N,g}$ . Among them, Eq. 9 was approximately solvable in the case of small batch gradient descent, where  $\mathbf{W}_{N,g}^T \mathbf{W}_{N,g} \bar{\mathbf{F}}_{N,k}$  was the characteristic of  $\bar{\mathbf{F}}_{N,k}$  according to the  $\mathbf{W}_{N,g} \bar{\mathbf{F}}_{N,k}$  map.

$$\max_{\mathbf{W}_{N,g} \mathbf{W}_{N,g}^T = \mathbf{I}} \frac{1}{M} \sum_{k=1}^M \|\mathbf{W}_{N,g}^T \mathbf{W}_{N,g} \bar{\mathbf{F}}_{N,k} - \bar{\mathbf{F}}_{N,k}\|_2^2 \quad (9)$$

In summary, to obtain  $\mathbf{W}_{N,g} (N = 1, 2, 3, \dots, 16)$ , we employed a small batch gradient descent approach to simultaneously compute  $\mathbf{W}_{N,g}$  in Eq. 9. During the  $t^{\text{th}}$  iteration of the gradient descent, we sampled a batch denoted as  $\beta_t$  for the following minimization problem, as presented in Eq. 10. We computed the gradient of the objective function to update  $\mathbf{W}_{N,g}$ . The batch size employed in this process was 8, and we trained  $\mathbf{W}_{N,g}$  for 200 epochs.

Using global eigenbases  $\mathbf{W}_{N,g} (N = 1, 2, 3, \dots, 16)$ , we were able to transfer information from the *reluN* layer of the source model *ENC* to the *reluN<sub>e</sub>* layer of the target model *enc*, as illustrated in Fig. 2(a).

$$\min_{\substack{\mathbf{W}_{N,g} \mathbf{W}_{N,g}^T = \mathbf{I} \\ N \in \{1, 2, 3, 4\}}} \frac{1}{|\beta_t|} \sum_{N=1}^4 \sum_{I_k \in \beta_t} \|\mathbf{W}_{N,g}^T \mathbf{W}_{N,g} \bar{\mathbf{F}}_{N,k} - \bar{\mathbf{F}}_{N,k}\|_2^2 \quad (10)$$

**Blockwise PCA-based KD.** To facilitate feature transformation within the distillation model, it was necessary to incorporate a paired decoder denoted as *dec*. This decoder worked in tandem with the encoder *enc* to extract input information effectively. The distillation method employed in this context was Principal Components Analysis (PCA).

The encoder *enc* was divided into a series of blocks  $\{enc_1, enc_2, enc_3, \dots, enc_{16}\}$ , where the output  $enc_N$  was the *reluN<sub>e</sub>* layer, and the decoder *dec* was divided into a group of blocks  $\{dec_{16}, \dots, dec_3, dec_2, dec_1\}$ , where the output  $dec_N$  was the *relu(N - 1)<sub>d</sub>* layer with the reproduction characteristics *relu(N - 1)<sub>e</sub>*. That was, the decoder took the *relu16<sub>e</sub>* features from *dec* as input to progressively reproduce the *relu16<sub>e</sub>*, ..., *relu3<sub>e</sub>*, *relu2<sub>e</sub>*, *relu1<sub>e</sub>* features and images. To implement our *enc - dec* model, we trained each pair of  $enc_N$  and  $dec_N$  with other pairs minimizing the distillation loss  $\mathcal{L}_{enc}^N$  of the encoder and the implementation loss  $\mathcal{L}_{dec}^N$  of the decoder. These four pairs were trained in order from  $N = 1$  to  $N = 16$ , as shown in Fig. 2(b), with  $enc_2$  and  $dec_2$  as examples.



In the distillation of the encoder, given the image  $I_k$ , we wanted to train the encoder block  $enc_N$  to make its decentralized output  $\bar{\mathbf{F}}_{N,k}^e$  close to the feature  $\mathbf{W}_{N,g}\bar{\mathbf{F}}_{N,k}$ . It was derived from the  $\bar{\mathbf{F}}_{N,k}$  map of the global eigenbases  $\mathbf{W}_{N,g}$  from the decentralized output of  $ENC_N$ , with reconstruction loss as shown in Eq. 11.

$$\mathcal{L}_{enc}^N(I_k) = \|\mathbf{W}_{N,g}^T \bar{\mathbf{F}}_{N,k}^e - \bar{\mathbf{F}}_{N,k}\|_2^2 \quad (11)$$

In the decoder implementation, given an image  $I_k$ , we wanted to approximate the output  $\mathbf{F}_{N-1,k}^d$  of the  $dec_N$  to the input image  $I_k$  in order to reproduce the input  $\mathbf{F}_{N-1,k}^e$  of the  $enc_N$  and the reconstructed image from the  $dec_1$ . In general, we minimized the  $I_{k_{rec}}$  formed by three regular terms, as shown in Eq. 12.

$$\mathcal{L}_{dec}^N(I_k) = \|\mathbf{F}_{N-1,k}^d - \mathbf{F}_{N-1,k}^e\|_2^2 + \|I_{k_{rec}} - I_k\|_2^2 + \|\mathbf{F}_{N,k_{rec}} - \mathbf{F}_{N,k}\|_2^2 \quad (12)$$

The third objective was to enable image reconstruction based on perceptual loss. It was noteworthy that when  $N = 1$ , the first term for feature reconstruction was absent. In summary, we had tackled the following optimization challenges during the training of  $encN$  and  $decN$ :

$$\min_{encN, decN} \mathcal{L}_{enc}^N(I_k) + \mathcal{L}_{dec}^N(I_k) \quad (13)$$

**Reducing channel lengths.** In accordance with the empirical principles of PCA dimensionality reduction, it was imperative to preserve the most vital information encapsulated in the channel length  $L_N^e$  of the target model  $enc$ . Specifically, the target layer  $reluN_e$  of  $L_N^e$  should retain variance information exceeding 85% of that found in the source layer  $reluN$ .

For each image  $I_k$  within our dataset, we calculated the covariance of its features (called  $\mathbf{F}_{N,k}$ ) extracted in the  $reluN$  layer. Let  $\sigma_{N,k}^j$  be the  $j^{th}$  largest eigenvalue of the covariance associated with the  $j^{th}$  principal eigenvector  $\mathbf{e}_{N,k}^j$ . The  $j^{th}$  explanatory variance,  $EV = \sigma_{N,k}^j / \sum_{\alpha=1}^{L_N} \sigma_{N,k}^\alpha$ , reflected the portion of the feature variance captured by  $\mathbf{e}_{N,k}^j$ , while the cumulative explanatory variance,  $CEV = \sum_{\beta=1}^{L'_N} \sigma_{N,k}^\beta / \sum_{\alpha=1}^{L_N} \sigma_{N,k}^\alpha$ , reflected the feature variance captured by the top  $L'_N$  feature vector. We used the mean cumulative explanatory variance (mCEV) to determine the value of  $L'_N$ . The mCEV, represented as the mean of the CEV values across all images, was expressed in Eq. 14.

$$\text{mCEV}(L'_N) = \frac{1}{M} \sum_{k=1}^M \frac{\sum_{\beta=1}^{L'_N} \sigma_{N,k}^\beta}{\sum_{\alpha=1}^{L_N} \sigma_{N,k}^\alpha} = \sum_{\beta=1}^{L'_N} \text{mEV}(\beta) \quad (14)$$

$$\text{mEV}(\beta) = \frac{1}{M} \sum_{k=1}^M (\sigma_{N,k}^\beta / \sum_{\alpha=1}^{L_N} \sigma_{N,k}^\alpha) \quad (15)$$

Where  $M$  was the number of images in the dataset, and  $\text{mEV}(\beta)$  was the mean  $\beta^{th}$  EV. We were looking for  $L'_N$  that meets  $\text{mCEV}(L'_N) \approx 85\%$ .

## Implicit Diffusion model

**Diffusion process.** The diffusion process referred to the process of gradually adding Gaussian noise to the data until the data became random noise. For the original data  $\mathbf{x}_0 \pi \sim q(\mathbf{x}_0)$ , each step of the diffusion process with a total of  $T$  steps was to add Gaussian noise to the data  $\mathbf{x}_{t-1}$  obtained in the previous step as follows:

$$q(\mathbf{x}_t | \mathbf{x}_{t-1}) = \mathcal{N}(\mathbf{x}_t; \sqrt{1 - \beta_t} \mathbf{x}_{t-1}, \beta_t \mathbf{I}) \quad (16)$$

Where  $\{\beta_t\}_{t=1}^T$  was the variance used for each step, which was between 0 and 1. For the diffusion model, we often called the variance of different steps the variance schedule or noise schedule. Usually, the latter step would adopt a larger variance, that was  $\beta_1 < \beta_2 < \dots < \beta_T$ . Under a designed variance schedule, if the number of diffusion steps was large enough, the final result  $\mathbf{x}_T$  would completely lose the original data and become random noise. Each step of the diffusion process generated noisy data  $\mathbf{x}_t$ . The whole diffusion process was also a Markov chain:

$$q(\mathbf{x}_{1:T}|\mathbf{x}_0) = \prod_{t=1}^T q(\mathbf{x}_t|\mathbf{x}_{t-1}) \quad (17)$$

**Reverse process.** The diffusion process entailed the introduction of noise to data, whereas the reverse process served the purpose of noise removal. In the context of the reverse process, the knowledge of the true distribution  $q(\mathbf{x}_{t-1}|\mathbf{x}_t)$  at each step was crucial. Starting from an initial random noise  $\mathbf{x}_T \sim \mathcal{N}(0, \mathbf{I})$ , the gradual denoising procedure culminated in the generation of a genuine sample. Consequently, it was evident that the reverse process also corresponded to the data generation process.

**Table A3.** Size and inference time of different models. Notes: DDPM = Denoising Diffusion Probabilistic Models and DDIM = Denoising Diffusion Implicit Models. The experiment was implemented in NVIDIA TESLA V100 32GB GPU. Size and inference time of different models. The latent dims are 64, the number of inference steps is 20, and the image size is 256. SD = Stable diffusion. Units: Parameter size (MB), Inference time (second/image) and KD ratio (%).

Model	Trainable params	Params size	Inference time	KD ratio
VGG-11	9,220,993	35.18	$1.80 \times 10^4$	-
VGG-16	14,715,201	56.13	$2.54 \times 10^4$	-
VGG-19	20,024,897	76.39	$2.89 \times 10^4$	-
UNet	31,037,698	118.48	$8.43 \times 10^2$	-
KD-VGG-11	49,897	0.19	$1.75 \times 10^4$	99.46
KD-VGG-16	164,425	0.63	$2.19 \times 10^4$	98.88
KD-VGG-19	260,100	0.99	$2.60 \times 10^4$	98.70
KD-UNet	14,673,253	55.97	$5.22 \times 10^2$	52.72
VAE	52,519,176	12.50	$1.21 \times 10^3$	-
GAN	67,876,224	258.95	$3.93 \times 10^2$	-
SD-V1.4	1,370,661,847	5228.66	1.07	-
SD-V1.5	1,370,661,847	5228.66	1.10	-
SD-V2.1	1,290,388,111	4922.44	1.01	-
DDPM	113,712,824	433.78	0.96	-
IDM	116,669,808	445.06	0.97	-
Ours-VGG-11	97,376,010	371.46	0.79	16.54
Ours-VGG-16	97,491,353	371.90	0.79	16.44
Ours-VGG-19	97,585,725	372.26	0.80	16.36

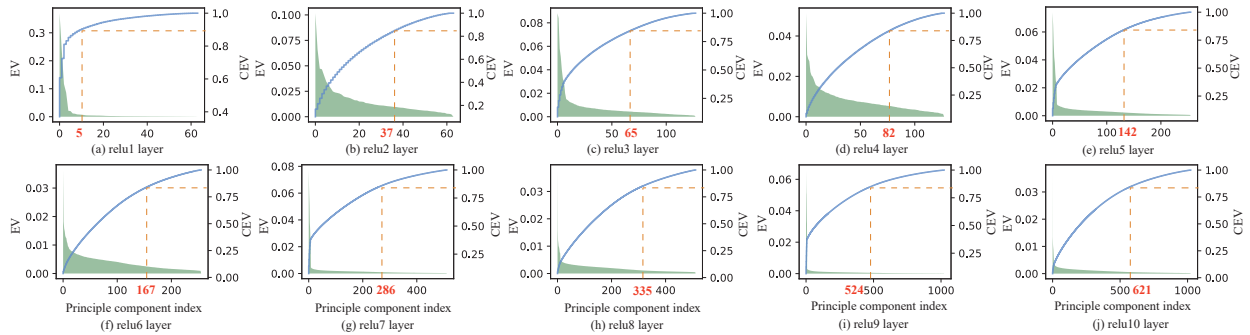


**Figure A1.** Features of UNet. Notes: Mean explained variance (green area) and mean cumulative explained variance (blue curve) of the *reluN* features.